

Electrical switching of chirality in rhombohedral graphene Chern insulators

Jing Ding^{1,2#}, Hanxiao Xiang^{1,2#}, Jiannan Hua^{1,2#}, Wenqiang Zhou^{1,2}, Naitian Liu^{1,2}, Le Zhang^{1,2},
Na Xin³, Kenji Watanabe⁴, Takashi Taniguchi⁵, Wei Zhu^{1,2}, Shuigang Xu^{1,2*}

¹ Key Laboratory for Quantum Materials of Zhejiang Province, Department of Physics, School of Science, Westlake University, 18 Shilongshan Road, Hangzhou 310024, Zhejiang Province, China

² Institute of Natural Sciences, Westlake Institute for Advanced Study, 18 Shilongshan Road, Hangzhou 310024, Zhejiang Province, China

³ Department of Chemistry, Zhejiang University, Hangzhou, 310058, China

⁴ Research Center for Electronic and Optical Materials, National Institute for Materials Science, 1-1 Namiki, Tsukuba 305-0044, Japan

⁵ Research Center for Materials Nanoarchitectonics, National Institute for Materials Science, 1-1 Namiki, Tsukuba 305-0044, Japan

[#]These authors contributed equally to this work.

*Correspondence to: xushuigang@westlake.edu.cn

Abstract:

A Chern insulator hosts topologically protected chiral edge currents with quantized conductance characterized by its Chern number. Switching the chirality of the Chern insulator, namely, the direction of the edge current, is highly challenging due to topologically forbidden backscattering but is of considerable importance for the design of topological devices. Nevertheless, this can be achieved by reversing the sign of the Chern number through a topological phase transition. Here, we report electrically switchable chirality in rhombohedral heptalayer graphene-based Chern insulators. The surface flat band and giant Berry curvature in rhombohedral multilayer graphene provide a highly tunable platform for engineering the topological states. By introducing moiré superlattices in rhombohedral heptalayer graphene, we observed a cascade of topological phase transitions at quarter electron filling of a moiré band. The Chern number can be continuously tuned from 0, -1, 1 to 2 by electric fields, manifesting as a large anomalous Hall effect and following Streda's formula. Sign reversal and the anomalous Hall effect also occurred at non-integer fillings, suggesting the possibility of electrically tunable topological phase transitions within the regime of fractional Chern insulators. Our work establishes rhombohedral heptalayer graphene moiré superlattices as a versatile platform for topological engineering. The realization of switchable chirality enhances the potential application of chiral edge currents in topological circuit interconnects.

Main text:

The interplay between nontrivial band topology and strong correlations produces exotic quantum states such as Chern insulators^{1,2}. A Chern insulator can support topologically protected dissipationless edge states, similar to those in the quantum Hall effect, but under zero magnetic field. This property has promising applications in low-power-consumption electronics and topological quantum computers^{3,4}. The Chern insulator is characterized by a quantized Hall resistance $\rho_{xy} = \frac{h}{Ce^2}$, where h is Planck constant, e is the elementary charge, and $C \neq 0$ is the Chern number. The Chern number C is a topological invariant defined by the integration of the Berry curvature over the entire Brillouin zone, characterizing the band topology⁵. The value of C determines the number of chiral edge states, while its sign determines the propagation direction of these edge states, or the chirality. In the conventional integer quantum Hall effect, electronic states form Landau levels under high magnetic fields, allowing C to be tuned consecutively from negative to positive values through changes in external magnetic fields or carrier density⁶. However, tuning C in a Chern insulator is generally challenging because the band topology is remarkably robust against external perturbations. Nevertheless, the ability to *in-situ* tune C , especially to reverse its sign, is crucial for realizing complex topological device architectures and holds promising applications in topological circuits⁷⁻¹⁰. To date, Chern insulators have been observed in several systems, including magnetically doped topological insulator thin film², MnBi_2Te_4 ¹¹, twisted graphene^{3,12}, $\text{WSe}_2/\text{MoTe}_2$ moiré superlattices¹³, twisted MoTe_2 ¹⁴⁻¹⁷, and rhombohedral graphene¹⁸⁻²⁴. However, *in-situ* switching the sign of nonzero C in these Chern insulators remains challenging.

Rhombohedral multilayer graphene has recently emerged as a promising platform for exploring correlated Chern insulators¹⁸⁻²³. The low-energy bands in rhombohedral multilayer graphene exhibit a unique power-law energy dispersion relation governed by $E \sim k^N$, where N is the layer number and k is the crystal momentum. This dispersion implies the presence of a rather flat band at low energy, with the flatness increasing with N , thus fostering strong correlations^{20-22,25-34}. Furthermore, the flat surface band in rhombohedral multilayer graphene possesses nontrivial topology with valley-contrasting Chern numbers that are tunable by an electric field, providing the essential ingredients for engineering correlated Chern states³⁵. When a moiré superlattice is introduced by aligning rhombohedral multilayer graphene to hexagonal boron nitride (h-BN), it hosts an isolated topological flat band with a nonzero Chern number. Consequently, Chern insulators with $C = 1$ and $C = 2$ have been reported in rhombohedral pentalayer¹⁸ and trilayer graphene¹⁹, respectively. However, switching the sign of C has not yet been achieved. Theoretical calculations suggest that the Chern states in rhombohedral graphene moiré superlattices can be effectively tuned by an electric field, with switchable C between multiple nonzero values³⁶.

In this work, we report the observations of Chern insulators in singly aligned rhombohedral heptalayer graphene/h-BN moiré superlattices. With the application of a large displacement field (D), we observe a cascade of topological phase transitions from trivial ($C = 0$) to several nontrivial states ($C = -1, 1, 2$) at the quarter electron filling of the moiré band, obeying Streda's formula. These versatile Chern states manifest as large anomalous Hall effect, ferromagnetism with hysteresis loops near zero field, and sign reversal in Hall signal at nonzero field. Notably, the topological phase transition from $C = -1$ to $C = 1$ indicates the chirality of the Chern insulators can be effectively

switched by electric fields. This switchable sign of C can extend to non-integer fillings, suggesting the potential for tunable fractional Chern insulators. Our observations demonstrate the highly tunable topological states in rhombohedral heptalayer graphene moiré superlattices.

Phase diagram of singly aligned moiré superlattices

Our device was fabricated using h-BN encapsulated rhombohedral heptalayer graphene, as shown in Fig. 1a. We employed dual-gate structures to independently tune the carrier density (n) and D . During the fabrication, the top h-BN was crystallographically aligned with graphene (see Methods). Figure 1d shows the $n - D$ map of the longitudinal resistance R_{xx} at a temperature $T = 50$ mK and $B = 0$ T. We observed multiple correlated insulators on the electron-doping side, exhibiting a remarkable asymmetry with respect to D . For $D > 0$, a cascade of insulating states appears at moiré filling factors of $\nu = \frac{n}{n_0} = 0, 1, 2, 3, 4$ (n_0 is the density corresponding to one electron per moiré unit cell). By comparison, for $D < 0$, strong insulating states are observed only at $\nu = 0$, with weak resistance peaks at $\nu = 1, 2$. This asymmetrical feature suggests a single alignment between graphene and h-BN (see Methods). The twist angle of the graphene/h-BN moiré superlattice is estimated to be 0.86° , derived from the carrier density at full filling ($\nu = 4$ at $D > 0$). Notably, compared to non-aligned devices, the layer antiferromagnetic (LAF) insulating states occurring near $n = 0$ cm⁻² and $D = 0$ V nm⁻¹ are absent in our singly aligned device (see Methods), indicating that the moiré potential weakens the coupling between the top and bottom layer^{22,28,30}. In contrast, LAF states are preserved in singly aligned pentalayer graphene devices¹⁸, suggesting that layer number significantly influences the electronic states in rhombohedral graphene superlattices. A similar absence of LAF was observed in doubly aligned rhombohedral heptalayer graphene (see Methods).

Although the moiré superlattice and large layer number in our devices seem to decouple the two surface layers, the moiré potential at the top interface can still influence the electronic states at the bottom interface even with large $|D|$. We found at the region between $D = -0.75$ V nm⁻¹ and $D = -0.95$ V nm⁻¹, where the electrons are polarized away from the moiré interface, the weak moiré potential acting on the distant surface can induce multiple topological phase transitions. In contrast, if the moiré potential is strong, either occurring on the $D > 0$ side (see Extended Data Fig. 5) or in a doubly aligned device, only topological trivial phases were observed³⁰.

Figure 1e and 1f show enlarged $n - D$ maps of symmetrized R_{xx} and anti-symmetrized Hall resistance R_{xy} at $-1.0 < D < -0.7$ V nm⁻¹, measured at $B = \pm 0.5$ T. At $\nu = 1$, we observed unusual large R_{xy} values, accompanied by local minima in R_{xx} . Additionally, the sign of R_{xy} reverses with increasing $|D|$, while maintaining their large absolute values. In the following sections, we focus on this region and demonstrate that these transitions arise from topologically nontrivial transitions involving changes in Chern numbers.

Anomalous Hall effect at $\nu = 1$

To identify the topological states at $\nu = 1$, we first fixed $D = -0.93$ V nm⁻¹ and scanned out-of-plane magnetic field B forward and backward. As shown in Fig. 2a, R_{xy} exhibits large value of over 10 k Ω when $|B| > 0.1$ T and a sharp sign reversal near zero field, which are the

characteristic of the anomalous Hall effect. A closer examination, as shown in the inset of Fig. 2a, reveals magnetic hysteresis loops, indicating that spontaneous valley polarization breaks time-reversal symmetry. The value of R_{xy} is nearly quantized to $\frac{h}{2e^2} \approx 13 \text{ k}\Omega$ at remarkably low B down to 0.1 T, suggesting the possible existence of a Chern insulator with $C = 2$ at this D .

When the displacement field is tuned to $D = -0.80 \text{ V nm}^{-1}$, the evolution of R_{xy} as a function of B changes dramatically, as shown in Fig. 2b. On the $B > 0$ side, R_{xy} first exhibits a negative value approaching $-10 \text{ k}\Omega$ at 0.06 T. Subsequently, it reverses sign at 0.3 T and shows a large positive value, reaching $8 \text{ k}\Omega$ at 0.5 T. On the $B < 0$ side, the evolution of R_{xy} is antisymmetric with respect to the positive side. Switching the direction of B can flip the magnetization, resulting in a predictable sign reversal of R_{xy} . However, the abrupt sign reversal at $|B| = 0.3 \text{ T}$ is quite nontrivial. Similar abnormal sign reversal in R_{xy} can also be observed at $D = -0.79 \text{ V nm}^{-1}$, as shown in Fig. 2c, within a large scan region of B . The tunability of D on the anomalous R_{xy} can be directly visualized by fixing $B = 0.5 \text{ T}$, as shown in Fig. 2d. The anomalously large R_{xy} switches from a positive value to a negative value at $D \approx -0.83 \text{ V nm}^{-1}$.

Electric field dependent Chern insulators

To unveil the origin of the anomalous R_{xy} and its tunability by D , we performed fan diagrams by measuring R_{xx} and R_{xy} as a function of ν and B at various fixed D . Figure 3 shows the fan diagrams in the vicinity of $\nu = 1$ at four representative values of D . Performance at other D can be found in Extended Data Fig. 7. The remarkable features in Fig. 3 are that at all four D , R_{xy} exhibits large values at low field regions fanning out from $\nu = 1$, accompanied by clear dips in R_{xx} . Additionally, R_{xy} reverses its signs at $B = 0$. The dispersions of the local maximum R_{xy} and the corresponding dips in R_{xx} as a function of B follow Streda's formula $\frac{\partial n}{\partial B} = C \frac{e}{h}$, yielding various values of C marked in Fig. 3³⁷.

The emergence of the hysteretic anomalous Hall effect and the extracted nonzero C utilizing Streda's formula are hallmarks of correlated Chern insulators^{21,38-44}. We exclude the possibility of quantum Hall states giving rise to the nonzero C for the following reasons. First, the presence of ferromagnetism states manifesting as magnetic hysteresis near $B = 0$ indicate that this system exhibits spontaneous time-reversal symmetry breaking. Second, at a given D , only specific Chern states emerge at low field regimes. This is significantly different from the quantum Hall states, where usually a series of C simultaneously appear, and high magnetic field is necessary to form the Landau levels. Indeed, we observe a series of quantum Hall states fanning out from $\nu = 0$ and $\nu = 1$, gradually appearing at $B > 4 \text{ T}$ (see Extended Data Fig. 4). Third, within the same device, at $D > 0$ side, we observe topological trivial states showing neither the abnormal large R_{xy} nor nonzero C (see Extended Data Fig. 5). This suggests the states at $D > 0$ host distinct topology from those at $D < 0$ side.

In Fig.3, we observe strikingly D -dependent Chern states. At $D = -0.76 \text{ V nm}^{-1}$, a Chern state with $C = -1$ dominates at low fields. Another Chern state with $C = 1$ gradually emerges at $B > 2 \text{ T}$. When decreasing D to -0.84 V nm^{-1} , the $C = 1$ state extends to low field region and wins in

the competition with $C = -1$ state at $B < 0.4$ T. Further decreasing D to -0.90 V nm⁻¹, a third Chern state with $C = 2$ emerges and participates in the competition. It dominates over the other two states at $B < 1$ T. The $C = -1$ is expelled to high field region, while $C = 1$ gradually smears. At $D = -0.92$ V nm⁻¹, the $C = 2$ state completely occupies the entire phase diagram. The coexistence of multiple Chern states with $C = -1, 1, 2$ and their competitions can also be observed by performing $\nu - D$ maps at fixed magnetic fields (see Extended Data Fig. 8-10). The cascade of topological phase transitions at $\nu = 1$ observed in our rhombohedral heptalayer graphene moiré superlattices differs from that in pentalayer graphene, where only $C = 1$ was observed¹⁸. The electric field tunability of multiple topological nontrivial states, especially the sign of nonzero C , offers a unique platform for topological engineering.

Anomalous Hall effect at non-integer fillings

Recent experiments on rhombohedral pentalayer graphene/h-BN moiré superlattice reported the observations of fractional quantum anomalous Hall states, which has stimulated great interest in this system^{18,45-50}. It is expected to explore more topological states in other layer numbers of rhombohedral graphene moiré superlattice. Our singly aligned rhombohedral heptalayer graphene/h-BN moiré superlattice exhibits a similar zero-field phase diagram (Fig. 1d) to that in the pentalayer system. Therefore, it is worth examining the anomalous Hall effect at non-integer fillings. As shown in Fig. 4a, besides the established Chern states at $\nu = 1$, we also observe anomalously large values of R_{xy} at $\nu < 1$ regions. Additionally, the sign of R_{xy} can be switched by a displacement field as that at $\nu = 1$. The anomalous Hall effect at non-integer fillings can be further confirmed by sweeping B forward and backward at various fixed ν , as shown in Fig. 4b, 4c, and 4d. The obvious magnetic hysteresis in Fig. 4b and 4d, as well as faint hysteresis in the inset of Fig. 4c, indicate time-reversal symmetry is spontaneously broken at non-integer fillings. Intriguingly, Fig. 4b and Fig. 4c exhibit distinct signs of R_{xy} at $B > 0$, suggesting they have opposite chirality. The sign of R_{xy} can be also switchable by finite B at $\nu = 0.68$, as shown in Fig. 4d. In general, Fig. 4 demonstrates the electric field tunable chirality can be extended to fractional filling regions ($\nu < 1$).

Discussion and outlook

Our findings of a cascade of topological phase transitions by simply tuning D reveal the fruitful topological phases in rhombohedral heptalayer graphene moiré superlattices. The incomplete quantization of R_{xy} at zero magnetic field may be attributed to several reasons. Unlike in pentalayer graphene¹⁸, where only one Chern insulator state was observed, multiple Chern insulator states exist in our system. At zero magnetic field, Chern insulators with various topologically nontrivial states ($C = -1, 1, 2$) and trivial states ($C = 0$) closely compete with each other in energy. As shown in Fig. 3, the Chern states are extremely sensitive to D . Even tiny spatial variations of D arising from non-uniform gating effects can result in different Chern states in adjacent domains. The multi-domain structure arising from the coexistence of multi-Chern states and incomplete equilibration of edge states with the contacts will prevent the observation of zero-field quantization⁵¹. Applied magnetic fields can localize disorder, facilitate the time-reversal symmetry breaking, and enlarge the topological nontrivial gaps, thereby improving quantization, as observed in magnetic topological insulators and magic-angle twisted bilayer graphene^{38-42,52-54}. There are also other possible reasons for the imperfect quantization. For example, interfacial charges induced disorders

or twist angle inhomogeneities may broaden the topological nontrivial gaps. The domains with slightly different twist angles form small grains, whose boundaries may be metallic or interfere with the edge states. Additionally, cooling down the electronic temperature may be crucial.

Although future studies with higher sample quality are necessary to unveil the full quantization of Chern insulators at strictly zero field, our findings already demonstrate that rhombohedral heptalayer graphene moiré superlattices provide a fertile platform for topological engineering. The Chern number-tunable Chern insulators can be used to design topological junctions. The multiple tuning knobs in rhombohedral graphene moiré superlattices, such as twist angle, alignment, and layer number, provide versatile routes to engineer their fertile topological phases. The emergence of $C = 2$ at $\nu = 1$ under large negative D , along with precursor features of fractional quantum anomalous Hall at $\nu < 1$, indicates the possible existence of high-order fractional quantum anomalous Hall states. The observation of Chern number switching can be used to create Chern junctions and design topological circuits, where Chern insulator domains with different Chern numbers can be controlled by fabricating multiple local gates⁷.

References:

- 1 Haldane, F. D. M. Model for a quantum Hall effect without Landau levels: condensed-matter realization of the "parity anomaly". *Phys. Rev. Lett.* **61**, 2015-2018 (1988).
- 2 Chang, C.-Z. *et al.* Experimental observation of the quantum anomalous Hall effect in a magnetic topological insulator. *Science* **340**, 167-170 (2013).
- 3 Polshyn, H. *et al.* Electrical switching of magnetic order in an orbital Chern insulator. *Nature* **588**, 66-70 (2020).
- 4 Lian, B., Sun, X.-Q., Vaezi, A., Qi, X.-L. & Zhang, S.-C. Topological quantum computation based on chiral Majorana fermions. *Proc. Natl. Acad. Sci. U.S.A.* **115**, 10938-10942 (2018).
- 5 Thouless, D. J., Kohmoto, M., Nightingale, M. P. & den Nijs, M. Quantized Hall conductance in a two-dimensional periodic potential. *Phys. Rev. Lett.* **49**, 405-408 (1982).
- 6 Klitzing, K. v., Dorda, G. & Pepper, M. New method for high-accuracy determination of the fine-structure constant based on quantized Hall resistance. *Phys. Rev. Lett.* **45**, 494-497 (1980).
- 7 Ovchinnikov, D. *et al.* Topological current divider in a Chern insulator junction. *Nat. Commun.* **13**, 5967 (2022).
- 8 Yuan, W. *et al.* Electrical switching of the edge current chirality in quantum anomalous Hall insulators. *Nat. Mater.* **23**, 58-64 (2024).
- 9 Zhang, C. *et al.* Manipulation of chiral interface states in a moiré quantum anomalous Hall insulator. *Nat. Phys.* (2024).
- 10 Schröter, N. B. M. *et al.* Observation and control of maximal Chern numbers in a chiral topological semimetal. *Science* **369**, 179-183 (2020).
- 11 Deng, Y. *et al.* Quantum anomalous Hall effect in intrinsic magnetic topological insulator MnBi₂Te₄. *Science* **367**, 895-900 (2020).
- 12 Serlin, M. *et al.* Intrinsic quantized anomalous Hall effect in a moiré heterostructure. *Science* **367**, 900-903 (2020).
- 13 Li, T. *et al.* Quantum anomalous Hall effect from intertwined moiré bands. *Nature* **600**, 641-646 (2021).
- 14 Park, H. *et al.* Observation of fractionally quantized anomalous Hall effect. *Nature* **622**, 74-79

- (2023).
- 15 Xu, F. *et al.* Observation of Integer and Fractional Quantum Anomalous Hall Effects in Twisted Bilayer MoTe₂. *Phys. Rev. X* **13**, 031037 (2023).
 - 16 Cai, J. *et al.* Signatures of fractional quantum anomalous Hall states in twisted MoTe₂. *Nature* **622**, 63-68 (2023).
 - 17 Zeng, Y. *et al.* Thermodynamic evidence of fractional Chern insulator in moiré MoTe₂. *Nature* **622**, 69-73 (2023).
 - 18 Lu, Z. *et al.* Fractional quantum anomalous Hall effect in multilayer graphene. *Nature* **626**, 759-764 (2024).
 - 19 Chen, G. *et al.* Tunable correlated Chern insulator and ferromagnetism in a moiré superlattice. *Nature* **579**, 56-61 (2020).
 - 20 Han, T. *et al.* Large Quantum Anomalous Hall Effect in Spin-Orbit Proximitized Rhombohedral Graphene. *Science* **384**, 647-651 (2024).
 - 21 Sha, Y. *et al.* Observation of a Chern insulator in crystalline ABCA-tetralayer graphene with spin-orbit coupling. *Science* **384**, 414-419 (2024).
 - 22 Han, T. *et al.* Correlated insulator and Chern insulators in pentalayer rhombohedral-stacked graphene. *Nat. Nanotechnol.* **19**, 181-187 (2024).
 - 23 Han, X. *et al.* Engineering the Band Topology in a Rhombohedral Trilayer Graphene Moiré Superlattice. *Nano Lett.* **24**, 6286-6295 (2024).
 - 24 Wang, S. *et al.* Chern Insulator States with Tunable Chern Numbers in a Graphene Moiré Superlattice. *Nano Lett.* **24**, 6838-6843 (2024).
 - 25 Zhou, H. *et al.* Half- and quarter-metals in rhombohedral trilayer graphene. *Nature* **598**, 429-433 (2021).
 - 26 Zhou, H., Xie, T., Taniguchi, T., Watanabe, K. & Young, A. F. Superconductivity in rhombohedral trilayer graphene. *Nature* **598**, 434-438 (2021).
 - 27 Shi, Y. *et al.* Electronic phase separation in multilayer rhombohedral graphite. *Nature* **584**, 210-214 (2020).
 - 28 Liu, K. *et al.* Spontaneous broken-symmetry insulator and metals in tetralayer rhombohedral graphene. *Nat. Nanotechnol.* **19**, 188-195 (2024).
 - 29 Han, T. *et al.* Orbital multiferroicity in pentalayer rhombohedral graphene. *Nature* **623**, 41-47 (2023).
 - 30 Zhou, W. *et al.* Layer-polarized ferromagnetism in rhombohedral multilayer graphene. *Nat. Commun.* **15**, 2597 (2024).
 - 31 Zhang, F., Jung, J., Fiete, G. A., Niu, Q. & MacDonald, A. H. Spontaneous quantum Hall states in chirally stacked few-layer graphene systems. *Phys. Rev. Lett.* **106**, 156801 (2011).
 - 32 Han, X. *et al.* Chemical Potential Characterization of Symmetry-Breaking Phases in a Rhombohedral Trilayer Graphene. *Nano Lett.* **23**, 6875-6882 (2023).
 - 33 Chen, G. *et al.* Evidence of a gate-tunable Mott insulator in a trilayer graphene moiré superlattice. *Nat. Phys.* **15**, 237-241 (2019).
 - 34 Chen, G. *et al.* Signatures of tunable superconductivity in a trilayer graphene moiré superlattice. *Nature* **572**, 215-219 (2019).
 - 35 Xiao, D., Yao, W. & Niu, Q. Valley-Contrasting Physics in Graphene: Magnetic Moment and Topological Transport. *Phys. Rev. Lett.* **99**, 236809 (2007).
 - 36 Zhang, Y.-H., Mao, D., Cao, Y., Jarillo-Herrero, P. & Senthil, T. Nearly flat Chern bands in

- moire superlattices. *Phys. Rev. B* **99**, 075127 (2019).
- 37 Streda, P. Theory of quantised Hall conductivity in two dimensions. *J. Phys. C: Solid State Phys.* **15**, L717-L721 (1982).
- 38 Nuckolls, K. P. *et al.* Strongly correlated Chern insulators in magic-angle twisted bilayer graphene. *Nature* **588**, 610-615 (2020).
- 39 Saito, Y. *et al.* Hofstadter subband ferromagnetism and symmetry-broken Chern insulators in twisted bilayer graphene. *Nat. Phys.* **17**, 478-481 (2021).
- 40 Das, I. *et al.* Symmetry-broken Chern insulators and Rashba-like Landau-level crossings in magic-angle bilayer graphene. *Nat. Phys.* **17**, 710-714 (2021).
- 41 Pierce, A. T. *et al.* Unconventional sequence of correlated Chern insulators in magic-angle twisted bilayer graphene. *Nat. Phys.* **17**, 1210-1215 (2021).
- 42 Choi, Y. *et al.* Correlation-driven topological phases in magic-angle twisted bilayer graphene. *Nature* **589**, 536-541 (2021).
- 43 Zhao, W. *et al.* Realization of the Haldane Chern insulator in a moiré lattice. *Nat. Phys.* **20**, 275-280 (2024).
- 44 Foutty, B. A. *et al.* Mapping twist-tuned multiband topology in bilayer WSe₂. *Science* **384**, 343-347 (2024).
- 45 Dong, Z., Patri, A. S. & Senthil, T. Theory of fractional quantum anomalous Hall phases in pentalayer rhombohedral graphene moiré structures. *arXiv*, arXiv:2311.03445 (2023).
- 46 Zhou, B., Yang, H. & Zhang, Y.-H. Fractional quantum anomalous Hall effects in rhombohedral multilayer graphene in the moiréless limit and in Coulomb imprinted superlattice. *arXiv*, arXiv:2311.04217 (2023).
- 47 Dong, J. *et al.* Anomalous Hall crystals in rhombohedral multilayer graphene I: interaction-driven Chern bands and fractional quantum Hall states at zero magnetic field. *arXiv*, arXiv:2311.05568 (2023).
- 48 Guo, Z., Lu, X., Xie, B. & Liu, J. Theory of fractional Chern insulator states in pentalayer graphene moire superlattice. *arXiv*, arXiv:2311.14368 (2024).
- 49 Kwan, Y. H. *et al.* Moiré fractional Chern insulators III: Hartree-Fock phase diagram, magic angle regime for Chern insulator states, the role of the moiré potential and goldstone gaps in rhombohedral graphene superlattices. *arXiv*, arXiv:2312.11617 (2024).
- 50 Xie, J. *et al.* Even- and Odd-denominator Fractional Quantum Anomalous Hall Effect in Graphene Moire Superlattices. *arXiv*, arXiv:2405.16944 (2024).
- 51 Tschirhart, C. L. *et al.* Imaging orbital ferromagnetism in a moire Chern insulator. *Science* **372**, 1323-1327 (2021).
- 52 Ge, J. *et al.* High-Chern-number and high-temperature quantum Hall effect without Landau levels. *Natl. Sci. Rev.* **7**, 1280-1287 (2020).
- 53 Cai, J. *et al.* Electric control of a canted-antiferromagnetic Chern insulator. *Nat. Commun.* **13**, 1668 (2022).
- 54 Xie, Y. L. *et al.* Fractional Chern insulators in magic-angle twisted bilayer graphene. *Nature* **600**, 439-443 (2021).

Methods

Device fabrication

Multilayer graphene was mechanically exfoliated from bulk natural graphite (Graphenium Flakes, NGS Naturgraphit) onto SiO₂ (285 nm)/Si substrates. The layer number of graphene flake was initially determined by optical contrast and further confirmed by transport measurements (see Extended Data Fig.3). Rhombohedral stacking domains were hunted by performing Raman maps of graphene. To stabilize the rhombohedral stacking orders in subsequent van der Waals assembly processes, we isolated them from Bernal stacking domains by a cutting process using a tungsten tip. The h-BN encapsulated rhombohedral graphene stacks were prepared using a standard dry transfer method with the assistance of poly(bisphenol A carbonate)/polydimethylsiloxane (PC/PDMS) stamp. During the transfer, we intentionally aligned one of the straight edges of top h-BN with that of the graphene (see Extended Data Fig. 1a) and misaligned them with that of the bottom h-BN, resulting in a single alignment configuration. The alive rhombohedral stacking domains in the final stacks were identified by a second Raman map, as shown in Extended Data Fig. 1d. We further used atomic force microscopy to select bubble free regions to make devices. For device fabrication, standard e-beam lithography, inductively coupled plasma, and e-beam evaporation were employed to design a multi-terminal Hall bar geometry. Contact electrodes were made by selectively etching the top h-BN and evaporating Cr/Au (3 nm/60 nm) on top of the exposed multilayer graphene.

Transport measurement

Low-temperature electronic transport measurements were conducted in a dilute refrigerator (Oxford Triton) with a base temperature of 50 mK. Standard low-frequency lock-in technique (SRS 830) at a frequency of 17.7 Hz was used to measure the longitudinal and Hall resistance of a Hall bar device. The AC excitation current was set to be 10 nA. Gate voltages were applied using a Keithley 2614B.

Dual-gate structures were utilized to independently tune the total carrier density n and the displacement field D . Their values were converted from the top gate (V_t) and bottom gate (V_b) voltages using a parallel plate capacitor model: $n = \frac{C_b \Delta V_b}{e} + \frac{C_t \Delta V_t}{e}$ and $D = \frac{C_b \Delta V_b - C_t \Delta V_t}{2\epsilon_0}$, where C_b (C_t) are the bottom (top)-gate capacitances per unit area, $\Delta V_b = V_b - V_b^0$ ($\Delta V_t = V_t - V_t^0$) are the effective bottom (top) gate voltages, e is the elementary charge, and ϵ_0 is the vacuum permittivity. C_b (C_t) were measured from the Hall effect at normal regions and calibrated by Landau level sequences at $\nu = 0$ (see Extended Data Fig. 4).

Symmetrized R_{xx} and anti-symmetrized R_{xy}

The measured Hall resistance R_{xy} inevitably contains signals from longitudinal resistance R_{xx} due to the imperfect Hall bar geometry. To eliminate the components of R_{xx} from R_{xy} , we used the standard procedure to obtain symmetrized R_{xy} and anti-symmetrized R_{xy} . For the data shown at a fixed B (such as Fig. 1e and 1f), we used: $R_{xy}(\pm B) = [R_{xy}(B) - R_{xy}(-B)]/2$ and $R_{xx}(\pm B) = [R_{xx}(B) + R_{xx}(-B)]/2$. For magnetic hysteresis data (such as Fig. 2a), we employed:

$$R_{xy}^{\text{antisym}}(B, \leftarrow) = [R_{xy}(B, \leftarrow) - R_{xy}(-B, \rightarrow)]/2 \quad \text{and} \quad R_{xy}^{\text{antisym}}(B, \rightarrow) = [R_{xy}(B, \rightarrow) - R_{xy}(-B, \leftarrow)]/2, \text{ where } \leftarrow \text{ and } \rightarrow \text{ indicate the magnetic field sweep direction.}$$

To show the Chern states under opposite directions of B , we present the raw data without symmetrization and antisymmetrization in fan diagrams (such as Fig. 3).

Band calculations

We firstly utilized the continuum model to calculate the single-particle band structure of singly aligned rhombohedral heptalayer graphene/h-BN moiré superlattice. We further considered electron-electron interactions using Hartree-Fock method. The details can be found in Supplementary Information.

Single alignment between graphene and h-BN

The crystallographical alignments between graphene and h-BN significantly affect the band structure of rhombohedral multilayer graphene. Due to the small lattice mismatch and similar crystal structure between graphene and h-BN, a moiré superlattice can form at their interface with a moiré wavelength of $\lambda = \frac{(1+\delta)a}{\sqrt{2(1+\delta)(1-\cos\theta)+\delta^2}}$, where $a = 0.246$ nm is the lattice constant of graphene, δ and θ are the lattice mismatch and twist angle between graphene and h-BN, respectively. The carrier density corresponding to the full filling of a moiré band is $n_s = 4n_0 = 4/A$, where $A = \sqrt{3}\lambda^2/2$ is the area of a moiré unit cell. The pre-factor of 4 arises from the four-fold degeneracy in graphene.

The single alignment configuration can be determined from transport results along with the optical image of the final stack. Extended Data Fig. 1a marks the relative angles between graphene and top h-BN and bottom h-BN. Obviously, our heptalayer graphene was aligned with top h-BN and misaligned with bottom h-BN.

The phase diagrams for rhombohedral heptalayer graphene with various alignment configurations are shown in Extended Data Fig. 2. In non-aligned device, there is a LAF state occurring near $n = 0$ cm⁻² and $D = 0$ V nm⁻¹. This state is absent in singly aligned and doubly aligned devices, indicating that the interfacial moiré potential decouples the layer interactions. Additionally, the critical displacement field required for entering into layer-polarized insulating states increases from 0.4 V nm⁻¹ in non-aligned device to 0.6 V nm⁻¹ in singly aligned device, and 0.9 V nm⁻¹ in doubly aligned device, further suggesting that the moiré potential can trap carriers at the interface. Furthermore, we find that the strength of moiré potential can significantly determine the band topology of rhombohedral graphene. As already demonstrated in previous work, the doubly aligned device exhibits trivial band topology on both $D > 0$ and $D < 0$ sides³⁰. In contrast, our singly aligned device shows a trivial band at $D > 0$ side (see Extended Data Fig. 5), while nontrivial band topology is observed at $D < 0$ side, as demonstrated in the main text.

Trivial topology at $D > 0$ side

Extended Data Fig. 5 shows the phase diagram on the $D > 0$ side. Resistive states in R_{xx} along with corresponding sign reversals in R_{xy} appear at all the fillings ($\nu = 0, 1, 2, 3, 4$). As shown in Extended Data Fig. 5a, there is no anomalously large R_{xy} across the entire phase diagram. The fan diagram exhibits only vertical lines in both R_{xx} and R_{xy} , indicating that all the states host $C = 0$ according to Streda's formula. It's noted that the large R_{xy} near integer fillings shown in Extended

Data Fig. 5c arises from the mixture of R_{xx} and vanishes after anti-symmetrization, as shown in Extended Data Fig. 5a.

Evolution of Chern state with magnetic fields.

The cascade of topological phase transitions at $\nu = 1$ can also be unveiled from $n - D$ maps at various fixed B , as illustrated in Extended Data Fig. 8- 10. At very low fields, such as $B = 0.1$ T and 0.2 T, Chern states with $C = 1$ and 2 occur close to $\nu = 1$. Above $B = 0.3$ T, a Chern state with $C = -1$ emerges from $D \approx -0.8$ V nm⁻¹ and gradually extends to high $|D|$ regions with increasing B . At high B (such as from 1.5 T to 3 T), the positions of different Chern states separate to different ν and are equally distributed away from $\nu = 1$. These features represent the typical dispersion behavior of topological nontrivial states governed by Streda's formula⁴⁴. At even higher B (such as 6.0 T), a series of quantum Hall states appears and starts to dominate over the three Chern states.

Acknowledgements:

This work was funded by National Natural Science Foundation of China (Grant No. 12274354, S.X.), the Zhejiang Provincial Natural Science Foundation of China (Grant No. LR24A040003, S.X.; XHD23A2001, S.X.), the R&D Program of Zhejiang province (Grant No. 2022SDXHDX0005, W.Z.), and Westlake Education Foundation at Westlake University. We thank Chao Zhang from the Instrumentation and Service Center for Physical Sciences (ISCPS) at Westlake University for technical support in data acquisition. We also thank Westlake Center for Micro/Nano Fabrication and the Instrumentation and Service Centers for Molecular Science for facility support. K.W. and T.T. acknowledge support from the JSPS KAKENHI (Grant Numbers 21H05233 and 23H02052) and World Premier International Research Center Initiative (WPI), MEXT, Japan.

Author Contributions

S.X. conceived the idea and supervised the project. J.D., H.X., and N.X. fabricated the devices. J.D. and H.X. performed the transport measurement with the assistance of W.Zhou, N.L. and L.Z.. J.H. and W.Zhu performed the band structure calculations. K.W. and T.T. grew h-BN crystals. S.X. wrote the paper with the input from J.D., H.X., N.X., and J.H.. All authors contributed to the discussions.

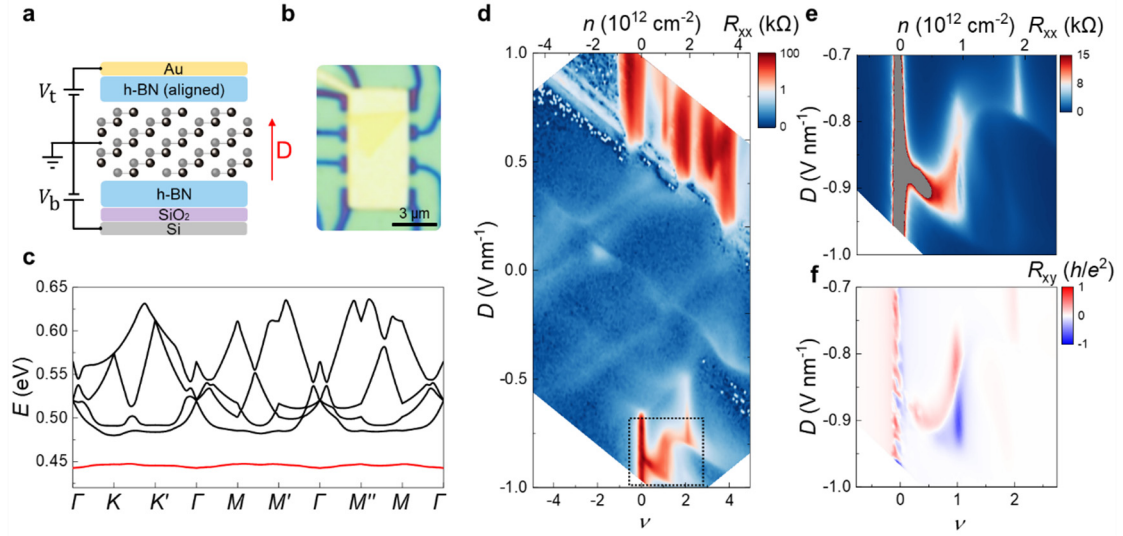


Fig. 1: Phase diagram of rhombohedral heptalayer graphene moiré superlattice. **a**, Schematic of device structure. The moiré superlattice was constructed at the interface between graphene and top h-BN. The red arrow illustrates the direction of positive D . **b**, Optical image of the final device with a standard Hall bar geometry. **c**, Topological flat band of rhombohedral heptalayer graphene moiré superlattices calculated based on Hartree-Fock method. The calculated Chern number of the isolated band (red color) has a nonzero number of 1, indicating the topological nontrivial characteristic. **d**, Longitudinal resistance R_{xx} as a function of filling factor ν and D at $B = 0$ T. Top x -axis labels the corresponding carrier density n . The black dashed box marks the region of interest in the main text. **e**, **f**, Zoomed-in phase diagram in the region marked by the black dashed box in **(d)**, plotted by the symmetrized R_{xx} (**e**) and anti-symmetrized Hall resistance R_{xy} (**f**) as a function of ν and D . The data were measured at $B = \pm 0.5$ T. At $\nu = 1$, anomalously large R_{xy} emerge with both positive and negative signs tunable by D . All the data were measured at base temperature $T = 50$ mK.

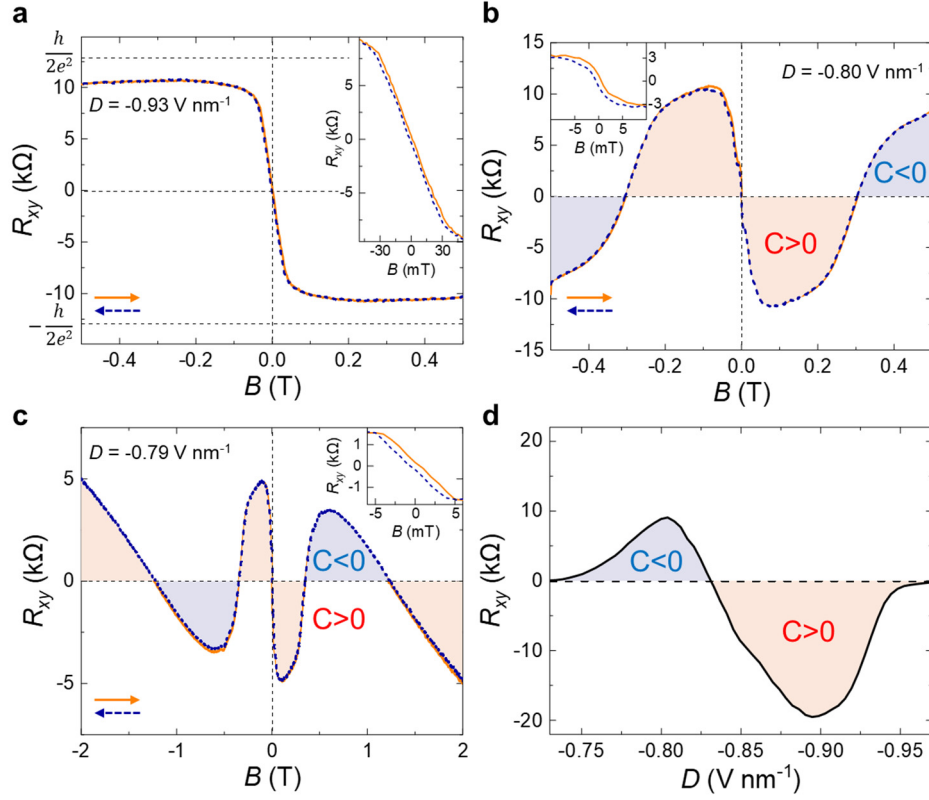


Fig. 2: Hysteretic anomalous Hall effect and chirality switching at $\nu = 1$. **a, b, c,** R_{xy} as a function of B swept forward (orange solid line) and backward (blue dashed line) at three representative displacement fields: $D_1 = -0.93 \text{ V nm}^{-1}$ (**a**), $D_2 = -0.80 \text{ V nm}^{-1}$ (**b**), $D_3 = -0.79 \text{ V nm}^{-1}$ (**c**). The insets at each panels show the corresponding enlarged views of the hysteresis loops at low field regions. At D_1 in (**a**), R_{xy} shows a plateaus-like feature approaching to $\pm h/2e^2$ when scanning B , corresponding to a Chern insulator of $|C| = 2$. At D_2 in (**b**) and D_3 in (**c**), multiple sign reversals of R_{xy} as a function of B can be observed, indicating the switching of the chirality of Chern insulators. **d,** Sign reversal of R_{xy} as a function of D at a fixed $B = 0.5 \text{ T}$. The corresponding signs of C are marked.

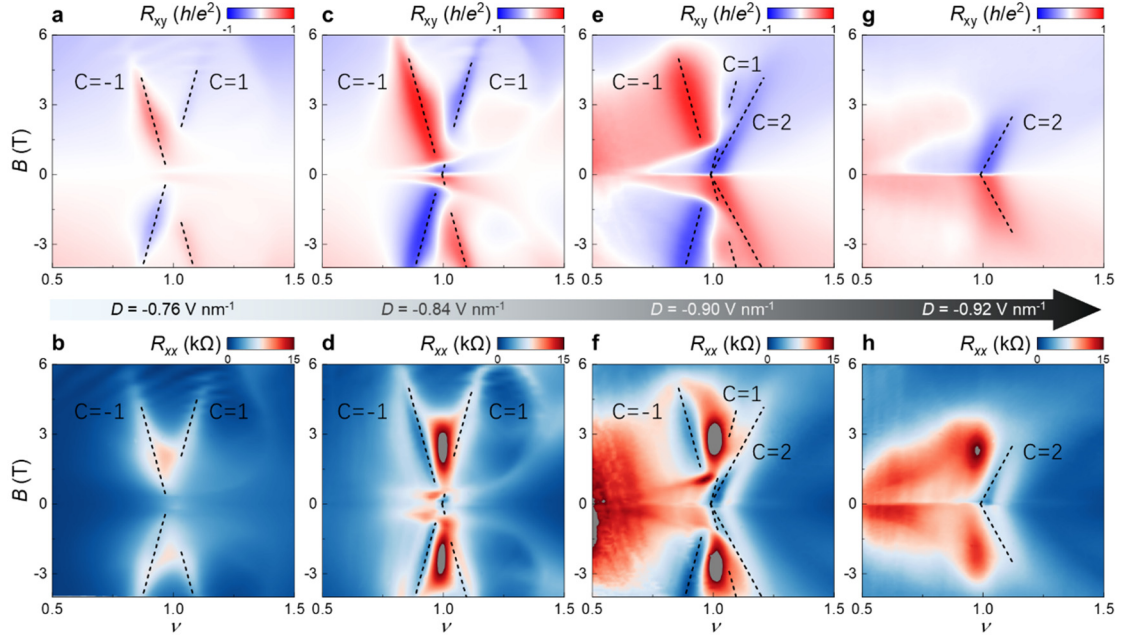


Fig. 3: Displacement field driven a cascade of topological phase transitions. **a, b**, R_{xy} (**a**) and R_{xx} (**b**) as a function of ν and B at a fixed $D = -0.76 \text{ V nm}^{-1}$. The dashed lines mark the Chern numbers of the topological nontrivial states $C = -1$ and $C = 1$. The $C = -1$ state dominates over $C = 1$ at low field region. **c, d**, R_{xy} (**c**) and R_{xx} (**d**) as a function of ν and B at a fixed $D = -0.84 \text{ V nm}^{-1}$. The $C = 1$ state wins the competition at low field region. **e, f**, R_{xy} (**e**) and R_{xx} (**f**) as a function of ν and B at $D = -0.90 \text{ V nm}^{-1}$. A third Chern state with $C = 2$ emerges from low field regions and participates the competition with the $C = 1$ and $C = -1$ states. **g, h**, R_{xy} (**g**) and R_{xx} (**h**) as a function of ν and B at $D = -0.92 \text{ V nm}^{-1}$. The Chern state with $C = 2$ wins the competition and dominates in the entire phase diagram. All Chen numbers are labeled according to the Streda's formula.

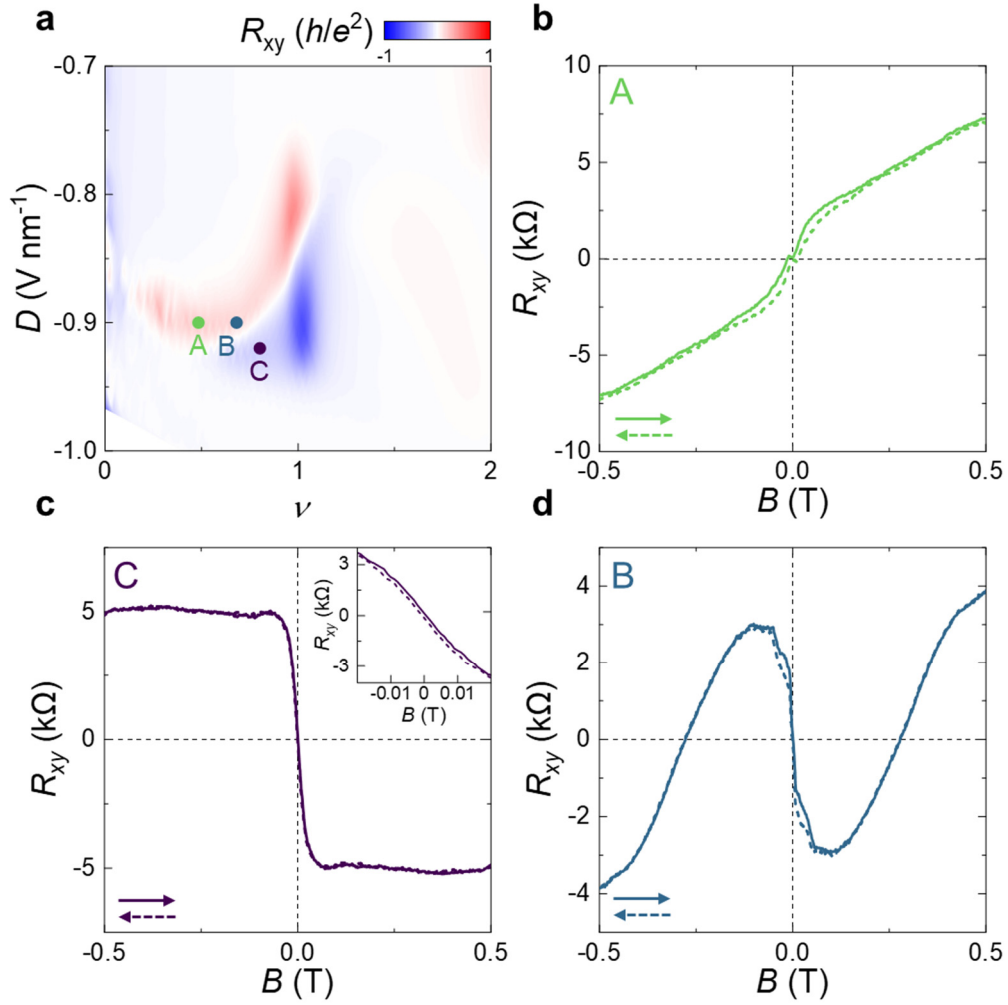
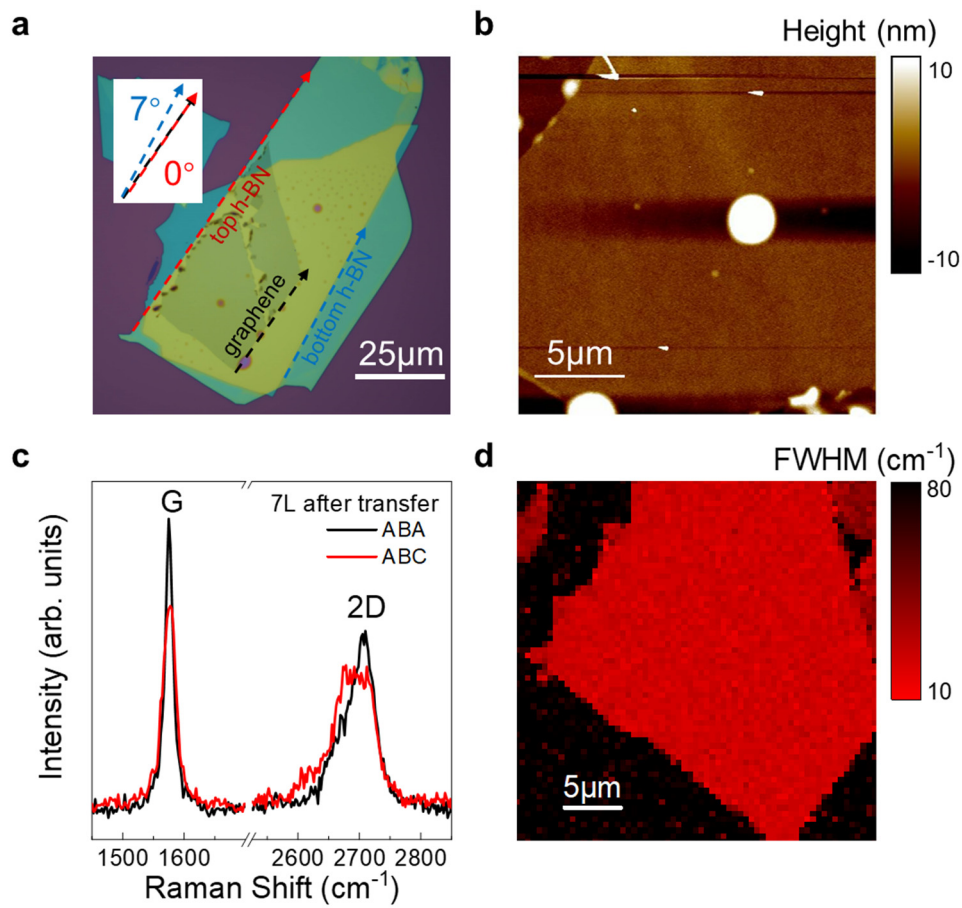
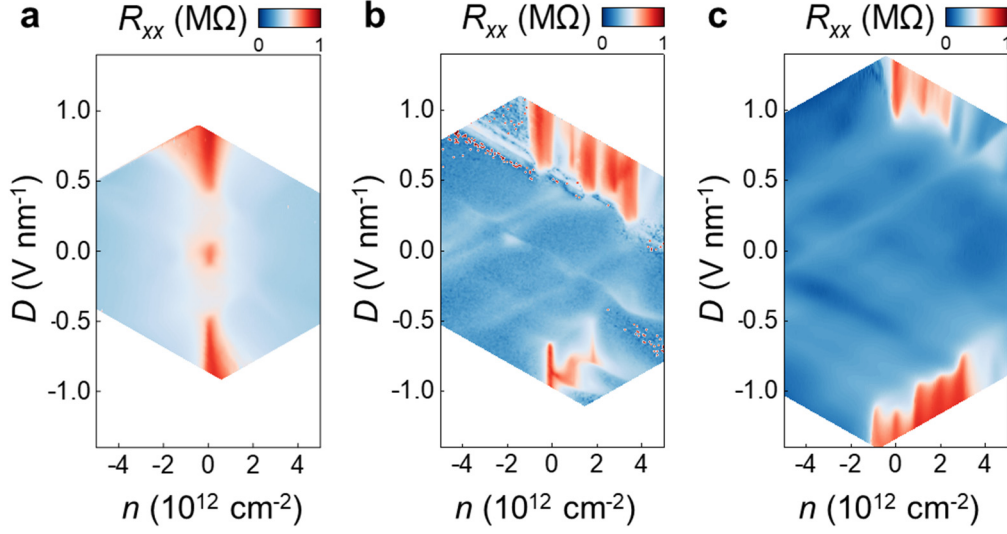


Fig. 4: Hysteretic anomalous Hall effect at non-integer fillings. **a**, Anti-symmetrized R_{xy} as a function of ν and D at $B = \pm 0.5$ T. Three representative regions are labeled: Position A ($\nu = 0.48, D = -0.90 \text{ V nm}^{-1}$), Position B ($\nu = 0.68, D = -0.90 \text{ V nm}^{-1}$), Position C ($\nu = 0.80, D = -0.92 \text{ V nm}^{-1}$). **b**, Hysteretic Hall signal at $\nu = 0.48$ marked by Position A in (a). **c**, Plateau-like and hysteretic anomalous R_{xy} at $\nu = 0.80$ marked by Position C in (a). The inset shows the enlarged view of the hysteresis loop at low field regions. **d**, R_{xy} with hysteresis and sign reversal when applying B at $\nu = 0.68$ marked by Position B in (a). Solid (dashed) line denotes that the sweep direction of B is forward (backward).

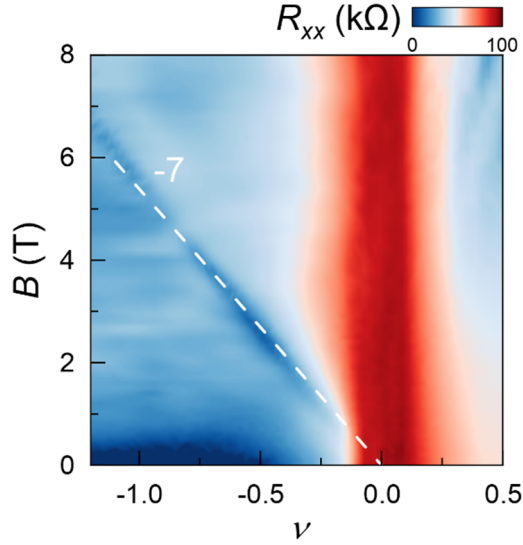


Extended Data Fig. 1: Optical image and Raman characterization of rhombohedral graphene.

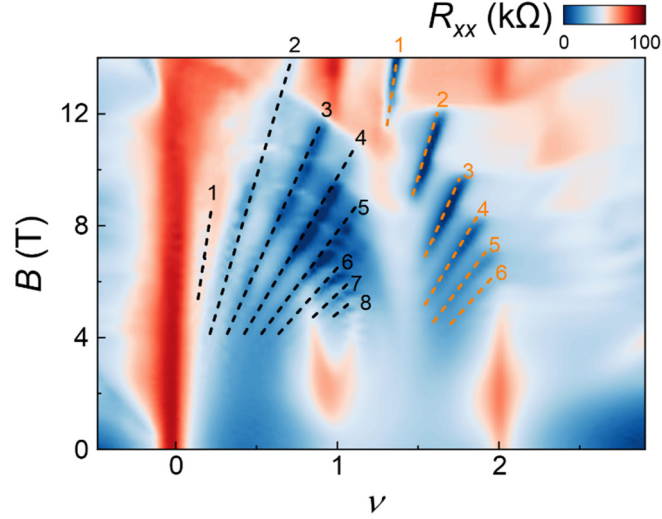
a, Optical image of the h-BN/graphene/h-BN heterostructure. The black, red, and blue dashed arrows mark the crystallographical edges of graphene, top, and bottom h-BN, respectively. The graphene was aligned to the top h-BN with the angle close to 0° , while the angle between graphene and bottom h-BN is about 7° . **b**, Atomic force microscopy image of the final stack. A large bubble-free region was selected to fabricate device. **c**, Raman spectra of rhombohedral stacking (red curve, denoted by ABC) and Bernal stacking (black curve, denoted by ABA) domains. **d**, Raman mapping of the full width at half maximum (FWHM) of 2D peak for the final stack. Nearly the entire isolated flake is rhombohedral stacking.



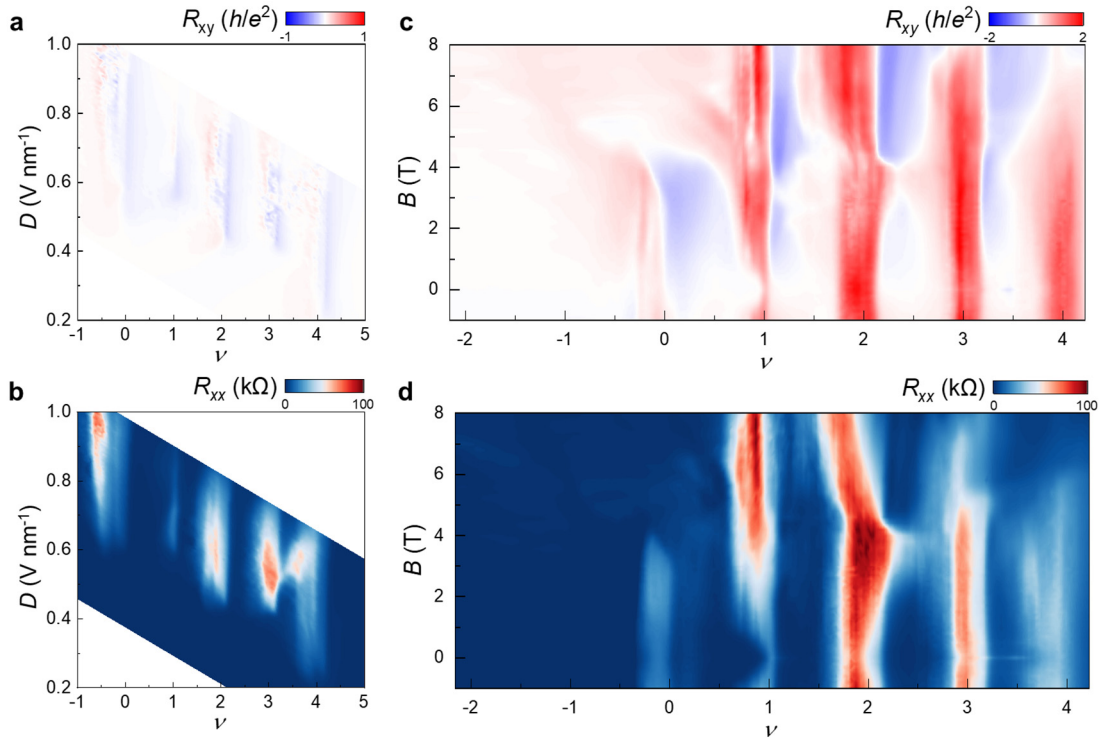
Extended Data Fig. 2: Comparison of phase diagrams for rhombohedral heptalayer graphene family. **a, b, c,** Color plots of R_{xx} as a function of ν and D for the intrinsic rhombohedral heptalayer graphene without moiré superlattices (**a**), with single moiré superlattices (**b**), and with double moiré superlattices (**c**). All the data were measured at $B = 0$ T and the base temperature $T = 50$ mK.



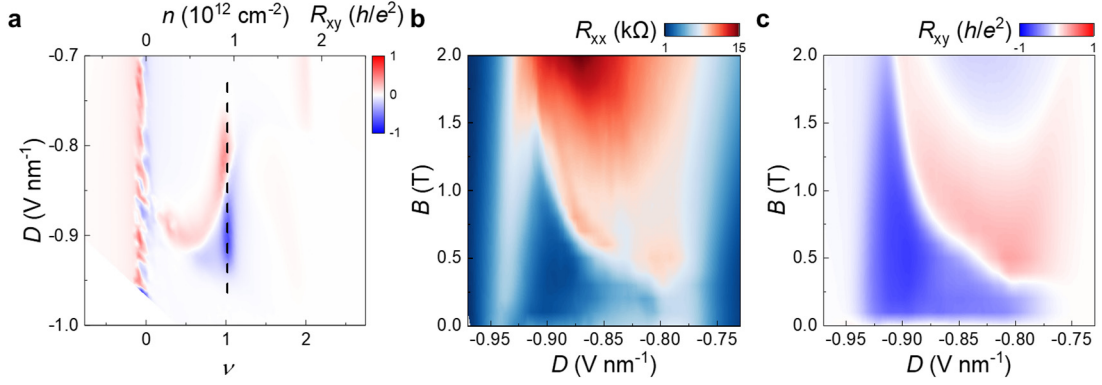
Extended Data Fig. 3: Layer identification of rhombohedral graphene from transport measurements. Fan diagram plotted by R_{xx} as function of ν and B at $D = -0.86$ V nm⁻¹ in the hole side region. A pronounced Landau level with a filling factor of $\nu_{LL} = -7$ is observed, corresponding to the layer-number dependent orbital degeneracy arising from the existence of 7π Berry phase in rhombohedral heptalayer graphene.



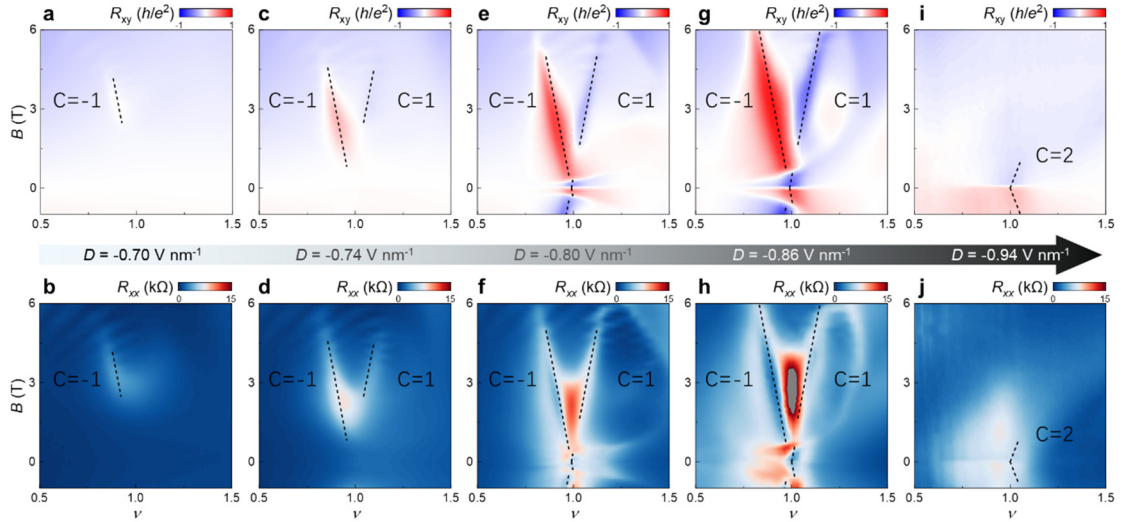
Extended Data Fig. 4: Landau quantization at high magnetic field. Landau fan diagram plotted by R_{xx} as a function of ν and B at fixed $D = -0.74 \text{ V nm}^{-1}$ in a large region of B . The black dashed lines mark the Landau level sequences fanning out from charge neutrality point ($\nu = 0$). The orange dashed lines mark the Landau level sequences fanning out from $\nu = 1$. Remarkable quantum Hall states emerge only when $B > 4 \text{ T}$. At low B , the phase diagram is dominated by Chern states.



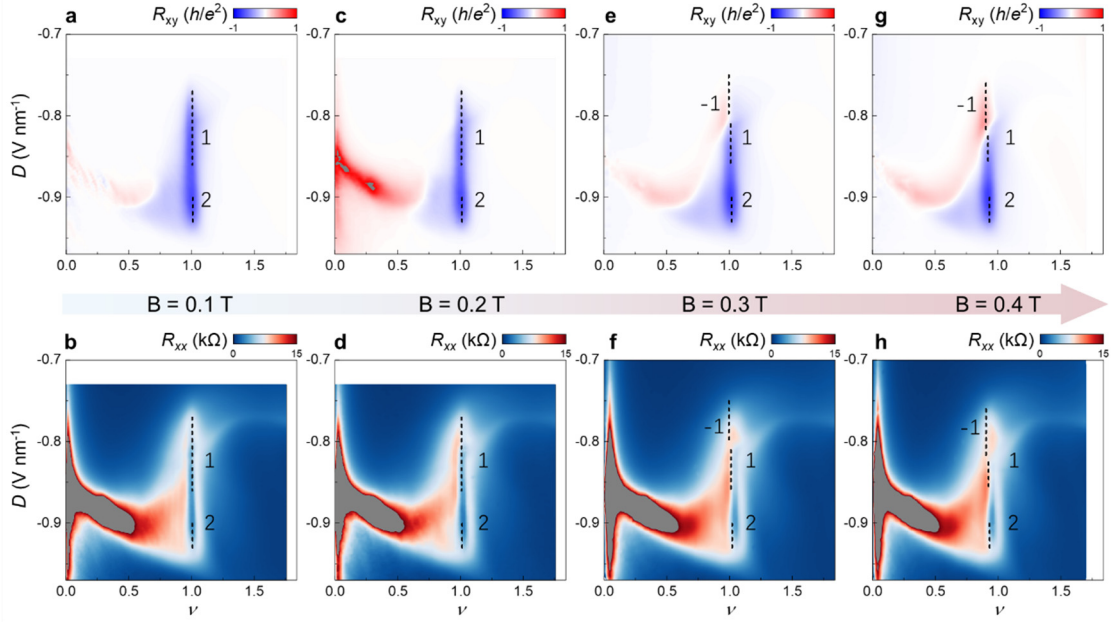
Extended Data Fig. 5: Trivial topology at $D > 0$ side. **a, b**, Color plots of symmetrized R_{xy} (**a**) and anti-symmetrized R_{xx} (**b**) as a function of ν and D at $B = \pm 0.5 \text{ T}$. **c, d**, R_{xy} (**c**) and R_{xx} (**d**) as a function of ν and B at fixed $D = 0.65 \text{ V nm}^{-1}$. Both (**c**) and (**d**) show only vertical peaks whose positions are independence of B . Therefore, all the correlated states are topologically trivial states according to Streda's formula.



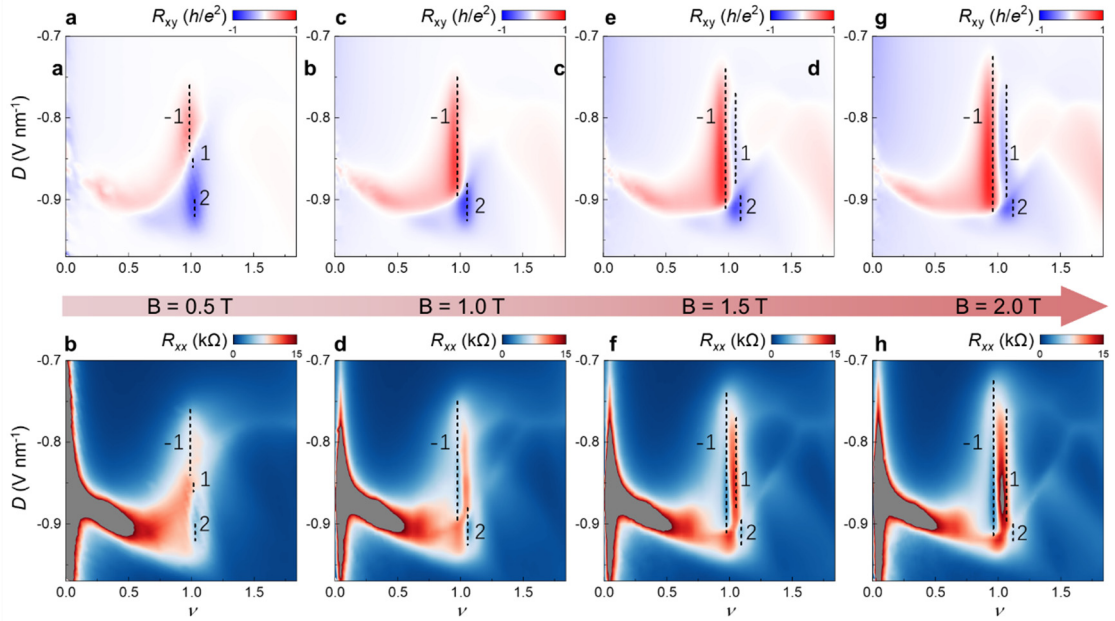
Extended Data Fig. 6: Chirality switching of Chern insulators at $\nu = 1$. **a**, Symmetrized R_{xy} as a function of ν and D at $B = \pm 0.5$ T. **b**, **c**, Color plots of R_{xx} (**b**) and R_{xy} (**c**) as a function of D and B at a fixed $\nu = 1$. The dashed line in (**a**) marks the sweep regions in (**b**) and (**c**).



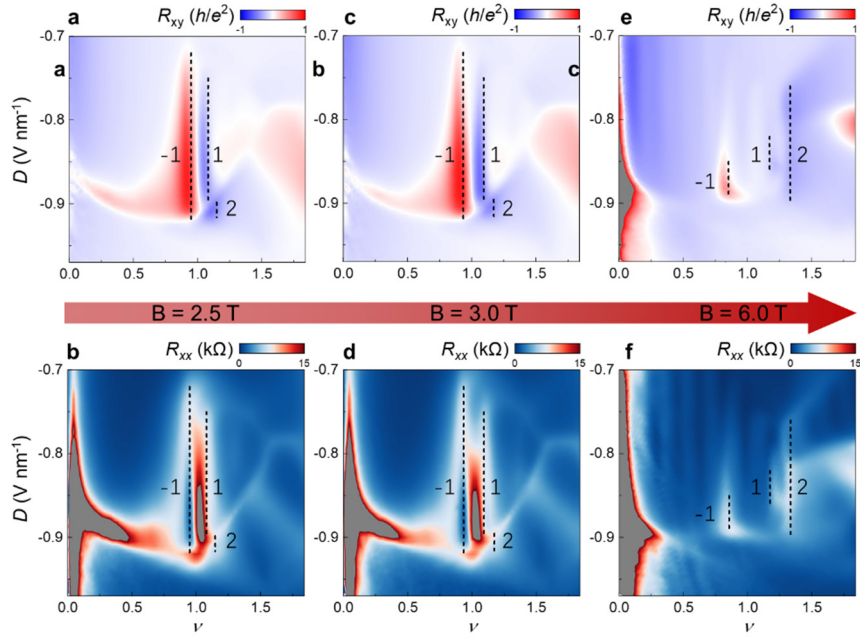
Extended Data Fig. 7: Additional data for the evolution of Chern states with various D . **a-j**, Color plots of R_{xy} (**a**, **c**, **e**, **g**, **i**) and R_{xx} (**b**, **d**, **f**, **h**, **j**) as a function of ν and B at $D = -0.70 \text{ V nm}^{-1}$ (**a**, **b**), $D = -0.74 \text{ V nm}^{-1}$ (**c**, **d**), $D = -0.80 \text{ V nm}^{-1}$ (**e**, **f**), $D = -0.86 \text{ V nm}^{-1}$ (**g**, **h**), $D = -0.94 \text{ V nm}^{-1}$ (**i**, **j**). Dashed lines mark the corresponding Chern states according to Streda's formula.



Extended Data Fig. 8: Evolution of Chern states with various B between 0.1 T to 0.4 T. a-h, Phase diagram plotted by symmetrized R_{xy} (a, c, e, g) and anti-symmetrized R_{xx} (b, d, f, h) as a function of ν and D at fixed $B = \pm 0.1$ T (a, b), ± 0.2 T (c, d), ± 0.3 T (e, f), ± 0.4 T (g, h). Dashed lines and numbers mark the topological nontrivial states with the corresponding Chern numbers.



Extended Data Fig. 9: Evolution of Chern states with various B between 0.5 T to 2.0 T. a-h, Phase diagram plotted by symmetrized R_{xy} (a, c, e, g) and anti-symmetrized R_{xx} (b, d, f, h) as a function of ν and D at fixed $B = \pm 0.5$ T (a, b), ± 1.0 T (c, d), ± 1.5 T (e, f), ± 2.0 T (g, h). Dashed lines and numbers mark the topological nontrivial states with the corresponding Chern numbers.



Extended Data Fig. 10: Evolution of Chern states with various B between 2.5 T to 6.0 T. a-f, Phase diagram plotted by R_{xy} (a, c, e) and R_{xx} (b, d, f) as a function of ν and D at fixed $B = \pm 2.5$ T (a, b), ± 3.0 T (c, d), ± 6.0 T (e, f). Dashed lines and numbers mark the topological nontrivial states with the corresponding Chern numbers.